Q. J. R. Meteorol. Soc. (2005), **131**, pp. 1607–1629 doi: 10.1256/qj.04.31

Accounting for unresolved clouds in a 1-D solar radiative-transfer model

By J. LI[1]*, S. DOBBIE[2], P. RÄISÄNEN[3] and Q. MIN[4]

[1]*Canadian Center for Climate Modeling and Analysis, Meteorological Service of Canada, Canada*
[2]*Institute for Atmospheric Science, School of the Environment, University of Leeds, UK*
[3]*Finnish Meteorological Institute, Finland*
[4]*ASRC, State University of New York at Albany, USA*

(Received 5 February 2004; revised 10 November 2004)

SUMMARY

New methods for the treatment of solar radiative transfer through overlapping and inhomogeneous clouds are presented. First, a new approach to cloud overlap is shown. For the adjacent cloud blocks, the traditional maximum overlap can be relaxed to a mixture of maximum and random overlap treatments for layers that are adjacent but not fully correlated. Second, a new radiative-transfer algorithm has been developed to deal with these various cloud overlap circumstances that is simple enough for implementation in a general-circulation model (GCM). When compared to appropriate benchmark calculations, we find that this new method can produce accurate results in heating rates and fluxes with relative errors generally less than 8%. Third, a new and very simple approach to treating radiative transfer through a cloud with horizontal subgrid-scale inhomogeneities is developed. This approach uses an optical-depth scaling technique to represent the subgrid-scale inhomogeneity. Finally, by combining all of the above elements, we provide a new algorithm for the combined treatment of cloud overlap and inhomogeneity and we show that it yields very reasonable accuracies for heating rates and fluxes. Through benchmark comparisons, we show that this new algorithm provides significant improvement over existing schemes in GCMs.

KEYWORDS: Cloud overlap Subgrid inhomogeneity

1. INTRODUCTION

Clouds greatly influence the radiative balance of the atmosphere (Liou 1986) and are integral in climate prediction (IPCC 1996, 2001; Morcrette and Jakob 2000). Yet, despite recent advances, their description in large-scale models is still crude (Jakob 2002).

The treatment of cloud overlap in general-circulation models (GCMs) is currently dominated by the random and maximum-random overlap techniques that were developed in previous decades (Manabe and Strickler 1964; Geleyn and Hollingsworth 1979; Jakob and Klein 1999; and others). A rigorous implementation of solar radiative transfer involving cloud overlap is difficult (Stubenrauch *et al.* 1997; Collins 2001; Räisänen *et al.* 2004) and can quickly exceed computational limits.

Historically, cloud overlap has been treated with the cloud matrix method which is used to handle the maximum-random overlap. Recently, however, the traditional concept of maximum-random overlap has been challenged by cloud-resolving model studies (e.g. Barker *et al.* 1999) and observations (Hogan and Illingworth 2000, 2003; Mace and Benson-Troth 2002). However, maximum-random overlap assumption aside, the cloud matrix method for handling the solar radiative transfer through a cloud system has never been rigorously validated. It is shown in the following sections that the cloud matrix method can give rise to significant errors.

An alternate method is the multi-column approach (Stubenrauch *et al.* 1997; Collins 2001; Räisänen *et al.* 2004), in which cloud fraction for each column is either 0 or 1, so treatment of cloud overlap is trivial and the results should be accurate. However, since calculations are performed individually for each column, the computational time can be a problem for the multi-column approach. In this paper a quasi multi-column approach

* Corresponding author: Canadian Center For Climate Modeling and Analysis, Meteorological Service of Canada, PO Box 1700, University of Victoria, Victoria, B.C., Canada V8P 2Y2. e-mail: Jiangnan.Li@ec.gc.ca

is proposed. The scheme has accuracy nearly as high as the multi-column scheme but it is more computationally efficient.

It is important that GCMs account not only for overlap but also for cloud inhomogeneity. A number of papers have been put forth to address this (Barker 1996; Oreopoulos and Barker 1999; Los and Duynkerke 2001; Li and Barker 2002; Kato 2003). We have found that a simple scaling of the cloud optical depth can properly account for the effects of subgrid-scale inhomogeneities. We find that the algorithm developed captures the details of cloud subgrid-scale variability sufficiently well.

2. Cloud matrix scheme

The results of the new algorithm outlined in section 3 will be contrasted with the cloud matrix scheme. Here we briefly outline the cloud matrix scheme (Harshvardhan *et al.* 1987; Liang and Wang 1997; Räisänen 1998; Li 2000; Bergman and Rasch 2002; and others) in order to highlight the physics which will be considered in our new scheme.

In the following we set level 1 as the top of the atmosphere (TAO) and level N as the surface. Layer i is between level i and level $i+1$. The cloud matrix elements $C_{l,m}$ give the total vertically projected cloud fraction between any two levels l and m. Furthermore, $c_i = C_{i,i+1}$ is the cloud amount in layer i, $C_{1,N}$ is total cloud fraction for the entire GCM column, and we set $C_{i,i} = 0$. We define a cloud layer as occupying one model layer and a cloud block as occupying one or more than one adjacent model layers. Different cloud blocks are separated by clear layers.

As shown in appendix A, two calculation paths for reflection and transmission are required to obtain the upward and downward fluxes at each model level k for solar radiative transfer. One path is from the TOA downward to the level k, and the other path is from the surface upward to the considered level k. Consequently, two sets of matrices are needed: one representing cloud overlap looking from the TOA downward to the level k, $C_{1,k}$, and the other looking upward from surface to the considered level k, $C_{N,k}$.

The radiative-transfer algorithm for the cloud matrix scheme used here is based on Bergman and Rasch (2002). The following radiative functions are determined for each level k, separately for the clear and cloudy part of the GCM column: the downward transmittance of layers above k for direct solar radiation, $T_{1,k}(\mu_0)$, μ_0 being the cosine of the solar zenith angle; the reflectance of layers above k for diffuse radiation, $R_{1,k}$; and the reflectance of layers below k for direct solar radiation, $R_{N,k}(\mu_0)$ and for diffuse radiation, $\overline{R}_{N,k}$. In what follows, superscripts c and o represent the clear sky and cloudy sky, respectively. The clear-sky reflection and transmission can be calculated following appendix A. The cloudy-sky part of the computations is, however, more complicated. Three contributions have to be accounted for in the computation of the cloud-weighted mean reflectance and transmittance: the case with clear air above and cloudiness below level k, the case with cloudiness above level k and clear air below, and the case with cloudiness both above and below level k.

To illustrate this, consider the schematic shown in Fig. 1. At level $k+1$, the downward direct transmission is determined from three regions I, II and III (see Fig. 1(b)),

$$\begin{aligned} T^{\mathrm{o}}_{1,k+1}(\mu_0) = \{&(C_{1,k+1} - c_k)T^{\mathrm{o;c}}_{1,k+1}(\mu_0) + (C_{1,k} - C_{1,k+1} + c_k)T^{\mathrm{o;o}}_{1,k+1}(\mu_0) \\ &+ (C_{1,k+1} - C_{1,k})T^{\mathrm{c;o}}_{1,k+1}(\mu_0)\}/C_{1,k+1}, \end{aligned} \tag{1}$$

where the first variable in the superscripts of $T^{\mathrm{c;o}}_{1,k+1}(\mu_0)$, $T^{\mathrm{o;c}}_{1,k+1}(\mu_0)$ and $T^{\mathrm{o;o}}_{1,k+1}(\mu_0)$ represents the clear or cloudy portion for $T_{1,k}(\mu_0)$ at the previous level k, and the second

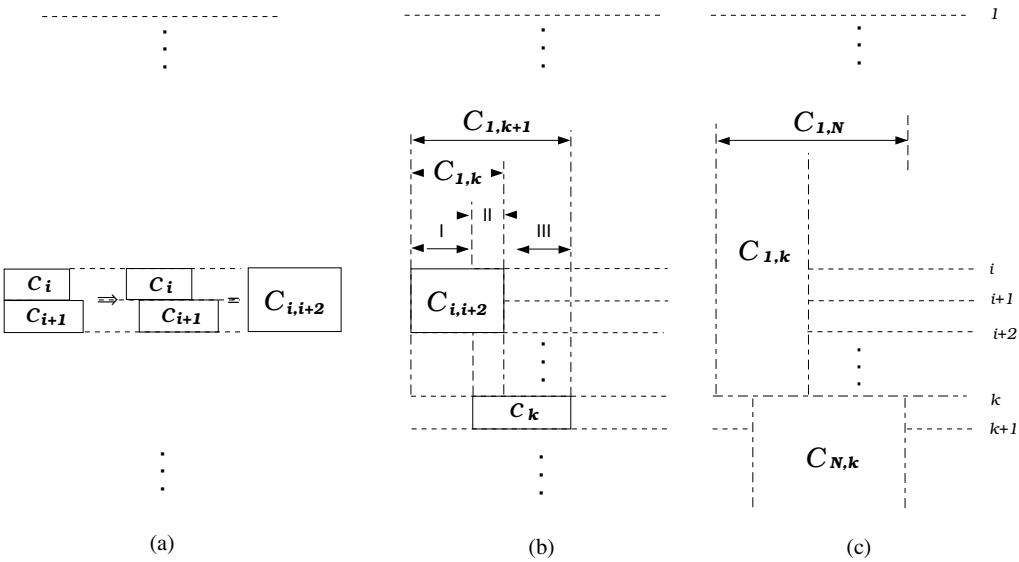

Figure 1. (a) A schematic of maximum overlap (left), relaxed maximum overlap (middle) and the corresponding cloud matrix element $C_{i,i+2}$ (right) for adjacent cloud layers i and $i+1$. (b) A schematic of relaxed maximum-random overlap. The cloud in layer k is randomly overlapped with the cloud block $C_{i,i+2}$ (and there are no other clouds above level k, so $C_{1,k} = C_{i,i+2}$). Regions I, II and III show the relationship between $C_{1,k}$ and $C_{1,k+1}$. (c) The matrix elements $C_{1,k}$, $C_{N,k}$ and $C_{1,N}$ needed to calculate radiative fluxes at level k in the cloud matrix method.

variable in the superscripts represents the clear or cloudy case for the added layer k (i.e. the layer transmissions and reflections, $\overline{t}_k$, $t_k(\mu_0)$, $\overline{r}_k$, and $r_k(\mu_0)$ refer to the clear or cloudy case, see appendix A). Similarly we can write down $\overline{R}^{\mathrm{o}}_{1,k+1}$. This process continues to the surface. Also, we need to calculate upward paths for $R^{\mathrm{o}}_{N,k}(\mu_0)$ and $\overline{R}^{\mathrm{o}}_{N,k}$ ($k = N, \ldots, 1$) in a similar way.

Finally, the downward flux at level k is obtained as (see Fig. 1(c))

$$F_k^- = f^{\mathrm{o;o}} F_k^{-\mathrm{o;o}} + f^{\mathrm{o;c}} F_k^{-\mathrm{o;c}} + f^{\mathrm{c;o}} F_k^{-\mathrm{c;o}} + f^{\mathrm{c,c}} F_k^{-\mathrm{c,c}}, \tag{2}$$

where

$$\begin{aligned} f^{\mathrm{o;o}} &= O_{C_{1,k};C_{N,k}} = C_{1,k} + C_{N,k} - C_{1,N}, \\ f^{\mathrm{o;c}} &= C_{1,k} - O_{C_{1,k};C_{N,k}} = C_{N,1} - C_{N,k}, \\ f^{\mathrm{c;o}} &= C_{N,k} - O_{C_{1,k};C_{N,k}} = C_{1,N} - C_{1,k}, \\ f^{\mathrm{c,c}} &= 1 - C_{1,N} \end{aligned}$$

represents the cloud fractional relation between the upward and downward paths; $O_{C_{1,k};C_{N,k}}$ represents the overlapping fraction of cloud above level k ($C_{1,k}$) and below it ($C_{N,k}$); $F_k^{-\mathrm{c;o}}$ is given by (A.9) with the downward path values of $T^{\mathrm{c}}_{1,k}(\mu_0)$ and $\overline{R}^{\mathrm{c}}_{1,k}$ for the clear-sky portion and with upward path values of $R^{\mathrm{o}}_{N,k}(\mu_0)$ and $\overline{R}^{\mathrm{o}}_{N,k}$ for the cloudy portion. Similarly $F_k^{-\mathrm{o;o}}$ is for the cloudy downward path and the cloudy upward path, and so on. Upward fluxes also consist of four contributions, analogously to (2).

3. QUASI MULTI-COLUMN (QMC) SCHEME

In section 5, it is shown that the cloud matrix method cannot accurately handle the radiative transfer for random overlap. In fact (2) does not describe the physics properly for random overlap of clouds. This is because, in the final calculation for the fluxes, (2) and Fig. 1(c) overly simplify the multiple-scattering process.

This difficulty can be overcome using the multi-column approach (Stubenrauch *et al.* 1997; Collins 2001; Räisänen *et al.* 2004). In the multi-column method, radiative-transfer calculations are performed for a set of columns. The columns are defined so that each layer inside a column has a cloud fraction of either 0 or 1. Thus, there is no cloud-fraction weighting problem in any column and accurate results should be obtained. The problem with the multi-column approach is it is time consuming since the number of columns required can be up to 2^N, where N is the number of non-adjacent cloud blocks.

(*a*) *Cloud overlap*

We first consider the computation of cloud fraction for adjacent cloud layers. Most GCMs assume maximum overlap, or perfect correlation, for adjacent cloud layers. So when there is cloudiness in two layers i and $i+1$, the combined cloud fraction for these layers is

$$C_{i,i+2} = c_i + c_{i+1} - O_{c_i;c_{i+1}} = \max(c_i, c_{i+1}), \tag{3}$$

where the overlapping portion is $O_{c_i;c_{i+1}} = \min(c_i, c_{i+1})$ (see the left part of Fig. 1(a)). However, since the cloud fraction for a model layer is the horizontal summation of all the clouds in the layer, the correlation between adjacent cloud layers is generally not perfect. This can be addressed by adding some random overlap components (Hogan and Illingworth 2000):

$$O_{c_i;c_{i+1}} = \alpha_i \min(c_i, c_{i+1}) + (1-\alpha_i) c_i c_{i+1}, \tag{4}$$

where $c_i c_{i+1}$ is the overlap region for random overlap and α_i is the cloud overlap parameter, between layers i and $i+1$. Since $c_i c_{i+1} \le \min(c_i, c_{i+1})$, $O_{c_i;c_{i+1}}$ in (4) is smaller than that in (3) for all $\alpha_i < 1$. Maximum overlap is therefore relaxed by allowing a random overlap component. We call this relaxed maximum (RM) overlap for adjacent clouds (see the middle part of Fig. 1(a)).

Now, assume that the mth cloud block consists of $n > 2$ layers $i, i+1, \ldots, i+n-1$. The total cloud fraction for such a cloud block, denoted as $\widetilde{C}_m = C_{i,i+n}$ is estimated here by applying (4) recursively. That is, for example the combined cloud fraction for layers i, $i+1$ and $i+2$ is computed as

$$C_{i,i+3} = C_{i,i+1} + c_{i+2} - \{\alpha_{i+1} \min(C_{i,i+2}, c_{i+2}) + (1-\alpha_{i+1}) C_{i,i+2} c_{i+2}\}. \tag{5}$$

This process is continued until the cloud fraction for the entire cloud block $C_{i,i+n}$ is obtained. Note that $C_{i,i+n} \ge \max(c_i, c_{i+1}, \ldots, c_{i+n-1})$, where the equality holds only when all $\alpha_l = 1$. Thus, $C_{i,i+n}$ is the relaxed maximum cloud fraction for such a block.

Observations (Hogan and Illingworth 2000) also show that non-adjacent cloud blocks adhere well to the random overlap rule, which means there is no vertical correlation between non-adjacent cloud blocks. Since RM overlap is assumed for adjacent cloud blocks, our entire overlap scheme can be denoted as 'relaxed maximum and random' (RMR) overlap. This should be more realistic than the widely used 'maximum-random overlap' assumption.

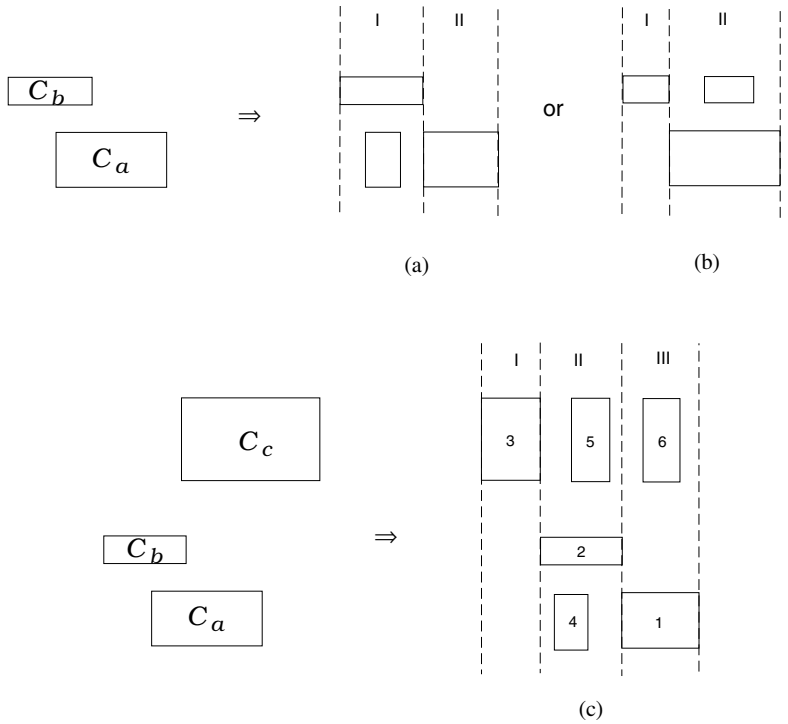

Figure 2. Top panels show the random overlap cloud system (C_a and C_b) being split into two regions I and II as (a) or (b); bottom panels show the random overlap cloud system (C_a, C_b and C_c) being split into three regions shown in (c).

(*b*) *Division of GCM column to subcolumns*

The multi-column approach consists of subdividing each GCM column into subgrid columns that are either overcast or clear at each level. This approach is modified here by limiting the number of subcolumns and by allowing subcolumns to contain fractionally cloudy layers under certain conditions. In this way, the number of columns can be considerably reduced without compromising the accuracy of the results significantly. Let us start with a simple case of two non-adjacent cloud blocks, C_a and C_b, as shown in Fig. 2(a). The total cloud fraction is

$$C = C_a + C_b - O_{C_a;C_b}. \tag{6}$$

If we restrict the cloud fraction to be either 0 or 1 in each column, four columns are needed. However, we can separate the whole cloud-covered area into two regions, I and II, as shown in Figs. 2(a) or (b). The area fractions for regions I and II are C_b and $C_a - O_{C_a;C_b}$ (Fig. 2(a)) or $C_b - O_{C_a;C_b}$ and C_a (Fig. 2(b)), respectively. In practice, it was found best to choose the columns so that within each column, the optically thickest cloud has a cloud fraction of 1. For example, if the upper cloud has a larger optical depth than the lower one, the pattern of Fig. 2(a) is chosen; otherwise the pattern of Fig. 2(b) is used.

Though partial cloudiness exists in region I of Fig. 2(a) and region II of Fig. 2(b), it is restricted entirely within the larger cloud domain. Regardless of where the smaller partial cloud is located within such a column, the radiative-transfer results are unchanged. Computation of radiative fluxes for these kinds of regions is discussed in section 3(c).

For a more general case with three cloud blocks, e.g. low, middle and high clouds, with corresponding cloud fractions C_a, C_b, and C_c, the cloud overlap pattern for C_a and C_b is the same as in Fig. 2(a). The third block C_c is divided into three parts, corresponding to its overlap pattern with the lower blocks (see Fig. 2(c)): region I, where C_c overlaps no other clouds; region II where it overlaps the optically thickest block C_b; and region III, where it overlaps C_a but not C_b. Thus, we have the cloud overlap pattern shown in Fig. 2(c) with six cloud blocks in three regions. The corresponding cloud fractions are

$$
\begin{aligned}
C_1 &= C_a - O_{C_a;C_b} = C_a \times (1 - C_b),\\
C_2 &= C_b,\\
C_3 &= C_c - O_{C_c;(C_a,C_b)} = (1 - C_a) \times (1 - C_b) \times C_c,\\
C_4 &= O_{C_a;C_b} = C_a \times C_b,\\
C_5 &= O_{C_c;C_b} = C_b \times C_c,\\
C_6 &= O_{C_c;(C_a,C_b)} - O_{C_c;C_b} = C_a \times (1 - C_b) \times C_c,
\end{aligned}
$$

where $O_{C_a;C_b}$ is the overlap region between C_a and C_b, $O_{C_c;C_b}$ is the overlap region between C_c and C_b, and $O_{C_c;(C_a,C_b)}$ is the overlapped region between C_c and the cloud coverage for the cloud system formed by C_a and C_b, i.e. $C_a + C_b - O_{C_a;C_b}$. The first form of the expressions for $C_1, \ldots, C_6$ is fully general and the second form comes from random overlap of separate cloud blocks.

Therefore, radiative fluxes are computed for only four subcolumns (for three cloudy regions as depicted in Fig. 2, and for the cloud-free region), as compared to $2^M = 8$ subcolumns for the multi-column approach. For this case, our method uses about 50% less computing time.

If there is another cloud block above C_c, the overlap becomes more complicated with an extra four possible patterns. It will complicate the radiation calculations and is probably not affordable for most climate models. We simply assume all clouds above C_c are randomly overlapped with C_c and form a single cloud block with C_c. Therefore only the solution corresponding to Fig. 2(c) is treated. It is shown that the case of more than three cloud blocks in a grid column seldom occurs in GCM simulations.

(*c*) *Radiative-transfer algorithm*

In QMC, the cloud system is split into 1–3 regions depending on the number of cloud blocks present. Radiative fluxes are computed for each region separately. There are two aspects to be considered. First, how to compute radiative transfer for individual cloud blocks; and second, how to combine the radiative fluxes for the entire column.

It is shown in section 5 that, while the cloud matrix method has difficulty with treating random overlap, it yields good results for individual cloud blocks when the layers within a block are close to maximum overlap. However, for the QMC scheme, three cloud matrices would be needed for detailed consideration of the cloud structure for each cloud block. We therefore propose a simpler method to deal with the cloud configuration within each cloud block.

We first compute the total cloud fraction $\widetilde{C}_m$ for each cloud block m using (5). The relationship between each layer inside the cloud block is then relaxed for the radiative-transfer calculations: the block cloud fraction $\widetilde{C}_m$ is used for each layer i within the block instead of its true cloud fraction c_i, and layer reflection and transmission are computed as cloud-fraction weighted mean values. For example, the direct transmission

for layer i within a cloud block of fraction $\widetilde{C}_m$ is

$$\langle t_i(\mu_o)\rangle = w_i t_i^{\mathrm{o}}(\mu_o) + (1 - w_i) t_i^{\mathrm{c}}(\mu_o), \tag{7}$$

where $w_i = c_i/\widetilde{C}_m$. The same applies to the layer's diffuse transmission $\overline{t}_i$ and direct and diffuse layer reflections $r_i(\mu_o)$ and $\overline{r}_i$, respectively. This approach resembles that employed by Stubenrauch *et al.* (1997), with the difference that those authors used cloud-fraction weighting of cloud optical depth, whereas we have weighted using single-layer reflection and transmission. A similar weighting method was analysed and applied in Fouquart and Bonnel (1980) and Morcrette and Fouquart (1986). We would like to emphasize our calculations show that (7) always generates better results compared to the method of cloud-fraction weighting of cloud optical depth.

To compute radiative fluxes for the different regions shown in Fig. 2(c), the following approach is used. First, for region I as well as for the clear part of the GCM column, fluxes can be computed simply as described in appendix A. For region III, the downward path quantities $\overline{R}_{1,k}$ and $T_{1,k}(\mu_0)$ are computed separately for the cloudy and clear parts of the region from the TOA to the top of the lower cloud layer. There, a weighted average is taken, i.e.

$$\overline{R}_{1,k} = w\overline{R}^{\mathrm{o}}_{1,k} + (1 - w)\overline{R}^{\mathrm{c}}_{1,k}, \tag{8}$$

where $w = C_6/C_1$ (see Fig. 2(c)). Below the top of the lower cloud layer, the calculation continues as a single path to the surface. Simple weighting by cloud fraction is valid here since the partial cloud is totally overlapped by the lower cloud. As mentioned for (1) and (2), cloud-fraction weighted results are generally invalid for random overlap cases. For the part of region III above the top of the lower cloud, the radiative fluxes are computed, for example, as

$$F_k^- = wF_k^{-\mathrm{o;o}} + (1 - w)F_k^{-\mathrm{c;o}}, \tag{9}$$

where the notations are the same as in (2).

For region II, a similar approach is taken. The downward path quantities $\overline{R}_{1,k}$ and $T_{1,k}(\mu_0)$ are separated into cloudy and clear paths from the TOA to the top of the middle cloud block (C_2), and the upward path quantities $\overline{R}_{N,k}$ and $R_{N,k}(\mu_0)$ are computed separately for cloudy and clear paths from the surface to the bottom of the middle cloud block.

(*d*) *Cloud subgrid-scale variability*

Accounting for cloud subgrid-scale variability, Barker (1996) specified the cloud water path probability density function with a gamma distribution function, and he obtained the single-layer transmission and reflection weighted by the gamma distribution in optical depth. This algorithm is based on the assumption that, whenever clouds occur in a model layer, the distribution of cloud (liquid or ice) water path $\mathcal{W}$ across the grid-cell can be described by

$$p_\gamma(\mathcal{W} \mid \langle\mathcal{W}\rangle, \nu) = \frac{1}{\Gamma(\nu)}\left(\frac{\nu}{\langle\mathcal{W}\rangle}\right)^{\nu} \mathcal{W}^{\nu-1}\, \mathrm{e}^{-\nu\mathcal{W}/\langle\mathcal{W}\rangle}, \quad \{\langle\mathcal{W}\rangle > 0;\ \nu > 0\}, \tag{10}$$

where $\langle\mathcal{W}\rangle$ is mean cloud water path, ν describes the width of the distribution, and $\Gamma(\nu)$ is the gamma function. As discussed in Li and Barker (2002), the distribution for optical depth is the same as the distribution for $\mathcal{W}$, provided the cloud droplet effective radius is constant within a grid cell.

The exact solution for radiative transfer through cloud with subgrid-scale variability is much more difficult for solar radiation in comparison with that for the infrared (Li 2002; Li and Barker 2002) because of the strong scattering present. Although the gamma-distribution-weighted transmission and reflection can be obtained for the downward and upward paths separately, similar to the infrared case, the vertical correlation cannot be properly addressed in the final equations for the fluxes. This is because the gamma-function-weighted mean results for the downward and upward paths cannot produce correct results for the flux with the upward and downward paths being properly matched. In other words, a larger liquid-water path (LWP) region in the downward path should correspond to a larger LWP region in the upward path, but this information is lost in the gamma-integral mean results for the reflection and transmission. Therefore the exact gamma-weighted solution for subgrid variability is difficult to obtain for solar radiation (Oreopoulos and Barker 1999; Kato, 2003).

If we neglect scattering (setting $\omega = 0$ in (A.4), the direct layer transmission becomes $\mathrm{e}^{-\tau/\mu_0}$, where τ is the optical depth. The gamma-function-weighted transmission is

$$\mathcal{T}(\langle\tau\rangle, \nu) = \int_0^\infty p_\gamma(\tau \mid \langle\tau\rangle, \nu)\, \mathrm{e}^{-\tau/\mu_0}\, \mathrm{d}\tau = \left(\frac{\nu}{\nu + \langle\tau\rangle/\mu_0}\right)^\nu \geq \mathrm{e}^{-\langle\tau\rangle/\mu_0}, \tag{11}$$

where $\langle\tau\rangle$ is the mean value of τ; this equals $\mathrm{e}^{-\langle\tau\rangle/\mu_0}$ only for $\nu \to \infty$ or $\langle\tau\rangle = 0$. Therefore, using the mean optical depth for the inhomogeneous cloud will underestimate the transmission. When scattering processes are included, the solution is much more complicated but the physics is the same. Therefore, in order to obtain accurate results accounting for the cloud subgrid variability but still based on the traditional radiative-transfer method shown in appendix A, the cloud optical depth has to be reduced. This has been realized before for various applications (Cahalan *et al.* 1994; Oreopoulos and Barker 1999).

Based on calculations for overcast clouds with various combinations of $\langle\tau\rangle$, ν and μ_0, we propose a simple empirical scheme of optical-depth adjustment. For layer k in a cloud block, the adjusted cloud optical depth is

$$\tau_k^* = \frac{\tau_k}{1 + 0.185(2 - \mu_0)^{0.4} f_\nu f_\tau}, \tag{12}$$

with

$$f_\nu = \frac{1}{1 + 5.68\nu^{1.4}}, \tag{13}$$

where ν is the minimum value for any layer within the cloud block (see the detailed discussion in Li and Barker 2002),

$$f_\tau = \tau_k + 9.2\sqrt{\sum_{j=i}^{k} \tau_j}, \tag{14}$$

i is the top layer of the cloud block and the summation in (14) is from the top layer of the cloud block to the considered layer k. The layer optical depth is reduced more for the lower layers in a cloud block since the difference in direct transmissions between $\mathcal{T}(\langle\tau\rangle, \nu)$ and $\mathrm{e}^{-\langle\tau\rangle/\mu_0}$ increases for increasing $\langle\tau\rangle$. Apart from this scaling of optical depth, radiative fluxes for inhomogeneous cloud fields are computed exactly in the same manner as in the homogeneous case.

4. Radiation model and benchmark calculations

The new model that combines RMR cloud overlap and horizontal cloud variability has been tested in a radiation algorithm employing the correlated-k distribution method for gaseous transmission (Li and Barker 2005). The cloud solar optical properties are based on Dobbie *et al.* (1999) for the liquid phase and Fu (1996) for the ice phase. The new radiative-transfer model was assessed using artificial atmospheres created by embedding synthetic cloud forms into a midlatitude summer profile (McClatchey *et al.* 1972). A surface albedo of 0.2 was assumed.

The benchmark results were calculated using the Independent Column Approximation (ICA). For cases involving random overlap of low, middle and high clouds (Figs. 4 and 7 and Tables 2 and 5), ICA was combined with a stochastic approach: N calculations were made by a 1-D column radiation model, so that the cloud fraction in each cloud block was set randomly either to 0 or 1 (clouds were assumed identical within a contiguous block). For each cloud block, the probability of choosing a cloud fraction of 1 is equal to the mean cloud fraction for that cloud block. The radiative-transfer code was then applied to each N columns (either clear or cloudy) and the results were averaged to produce the fluxes and the profile of heating rates for the random cloud system. This method is equivalent to a 1-D Mont Carlo simulation, since the results are a statistical average of a random set of clouds. The standard deviation for the 1-D Mont Carlo simulation is therefore proportional to $N^{-1/2}$. Thus, a relatively large N (generally $N > 10\,000$), is required in order to obtain sufficiently high statistical accuracy.

The radiative treatment of subgrid variability for overcast clouds is performed numerically by utilizing a gamma weighting function for the cloud variability and performing the calculations for 10 000 points over the distribution. The result is obtained by the numerical integration of these results. For broken cloud fields, we use the 1-D bounded cascade model (Cahalan *et al.* 1994) to create the cloud field with subgrid-scale variability and we compute the radiative properties using these distributions. Results are obtained again by numerical integration of the radiative properties for this case. All the subgrid cloud cases are the same as those in Li and Barker (2002) for the infrared, the details for how to generate subgrid cloud field by using the cascade mode are shown in that paper.

5. Results

(*a*) *Cloud overlap for homogeneous clouds*

We first consider the radiative transfer through a single cloud block with various cloud configurations. In Fig. 3, the clouds are resolved into several identical sublayers (each 250 m thick). The shaded areas indicate the cloud configurations and the values inside the shaded areas indicate the cloud fraction. For high clouds each two neighbouring model layers are with the same cloud fraction. Cases A—D are cloud configurations with maximum overlap and case E exhibits slantwise overlap.

Low clouds are positioned from 1.0 to 2.0 km with a liquid-water content (LWC) of 0.22 g m^{-3} and an effective radius (r_e) of 5.89 μm. The middle clouds are positioned from 4.0 to 5.0 km with LWC = 0.28 g m^{-3} and $r_e = 6.2$ μm. Lastly, the high clouds are positioned from 10 to 12 km with an ice-water content (IWC) of 0.0048 g m^{-3} and a mean effective size (D_e) of 30 μm. The visible optical depth is $\tau \approx 60$, 72 and 0.49 for the low, middle and high cloud, respectively.

The cloud matrix method produces very accurate heating-rate results for all cases in Fig. 3, with relative errors generally less than 5%. In Table 1 it is shown that the

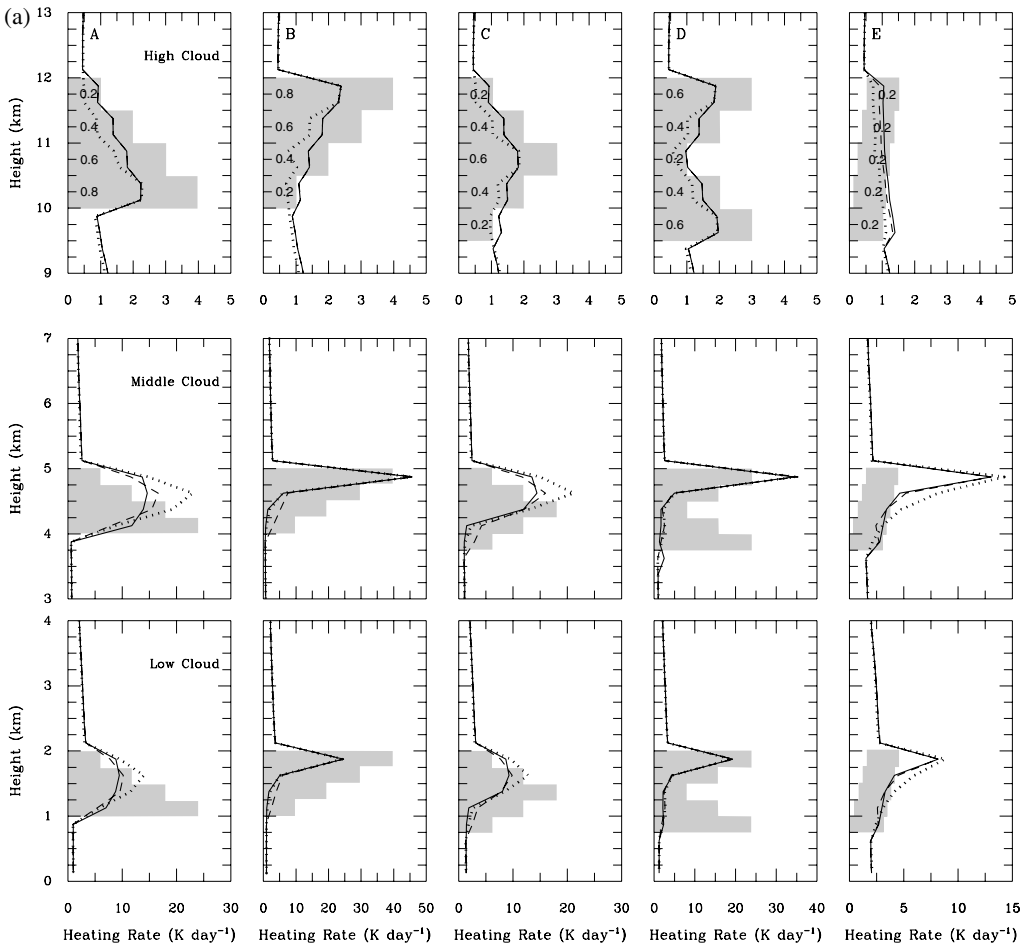

Figure 3. Heating-rate profiles for clouds with maximum overlap (cloud configurations of A–D) and for clouds with slant-wise overlap (configuration E). The numbers in the shaded areas show the cloud fractions. The solid lines are the benchmark results based on independent column approximation calculations, the dashed lines are the results for the cloud matrix method, and dotted lines are the results for the simplified scheme (7). Solar zenith angle is (a) 0° and (b) 60°. Each model layer is 250 m thick, and for high clouds every two neighbouring model layers have the same cloud fraction.

corresponding errors for upward fluxes at the TOA and downward fluxes at the surface are also small, relative errors being usually below 3%.

For the QMC method with the simple approximation given in (7), the accuracy of heating rates varies from case to case. Let us first examine the cases with low and middle clouds. For the cases A and C, the errors are relatively large, but for the other three cases, (7) produces results that are similar to the cloud matrix method. In cases A and C, where cloud fractions are smaller near cloud top than lower down, the use of cloud-fraction weighted transmission and reflection according to (7) enhances the transmission and reduces the reflection in such layers, but the reduction is bigger than the enhancement (see Table 1), which leads to more energy being held. Therefore, heating rates are overestimated in the upper and middle parts of the cloud although not in the uppermost layer. This also is related to overestimated enhancement of cloud absorption due to multiple scattering within the cloud. In cases B and D, where cloud fraction is

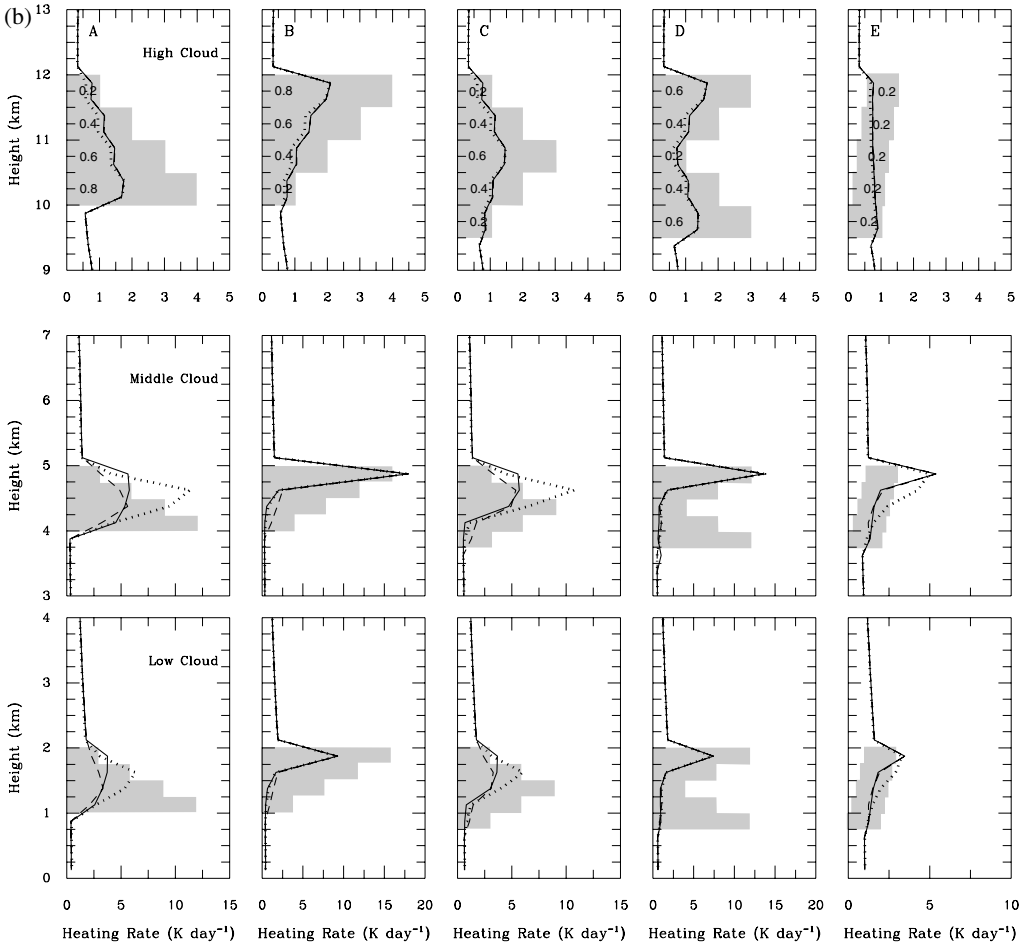

Figure 3. Continued.

largest in the top layer, heating rates are very accurate in the upper parts of the cloud. Below cloud top, the heating rates are generally small because the upper layers deplete the solar energy reaching the lower layers. For these cases the errors in absolute heating rate are small.

For high clouds, as for the cases with low and middle clouds, cases A and C are less accurate than cases B and D for heating rates, especially in the upper parts of the cloud. But since the high cloud is optically thin, solar energy can easily penetrate into the lower regions of the cloud. Heating rates are underestimated in the lower regions of the cloud for cases B and C, particularly when the solar elevation is high (Fig. 3(a)). Table 1 lists the radiative-flux errors at the TOA and at the surface also for the simple approximation given by (7). Generally the relative errors are less than 5%.

Overall, the accuracy of using (7) is reasonably good even for the detailed cloud structures considered in Fig. 3. This demonstrates that (7) can perform well both for cases with $\alpha_i = 1$ (i.e. maximum overlap cases A–D) and $\alpha_i < 1$ (case E). In case E, $\widetilde{C}_m$ in (7) was determined by setting $\alpha_i = \exp(-d_i/l)$, where d_i is the distance between layers i and $i+1$, and the decorrelation length is $l \approx 2.7$ km following (4).

TABLE 1. UPWARD AND DOWNWARD FLUXES (W m^{-2}) AT THE TOA AND AT THE SURFACE FOR CLOUDS AT THREE ALTITUDES AND FIVE OVERLAP CONFIGURATIONS (LABELLED A THROUGH E), FOR SOLAR ZENITH ANGLES 0° AND 60°. FIGURE 3 ILLUSTRATES THE FIVE CLOUD CONFIGURATIONS. FOR EACH CLOUD CASE THE VALUES IN THE LEFT COLUMN ARE BENCHMARK RESULTS, THE VALUES (IN PARENTHESES) IN THE FIRST ROW OF THE RIGHT COLUMN ARE ERRORS FOR THE CLOUD MATRIX METHOD COMPARED TO THE BENCHMARK, AND THE VALUES (IN PARENTHESES) IN THE SECOND ROW OF THE RIGHT COLUMN ARE ERRORS FOR THE QMC METHOD.

Cloud	A	B	C	D	E
			F^+ at TOA		
			$\theta^0 = 0$		
High	249.7 (−0.1)	249.7 (−0.1)	249.4 (−0.1)	250.3 (−0.1)	248.3 (−0.6)
	(−3.8)	(−3.7)	(−5.7)	(−2.9)	(−3.5)
Middle	750.9 (11.8)	754.3 (−4.0)	622.0 (19.3)	657.5 (9.0)	445.9 (1.3)
	(−36.1)	(−16.9)	(−18.6)	(−3.1)	(−36.1)
Low	684.9 (11.8)	691.5 (−2.3)	581.6 (12.3)	616.6 (3.2)	422.1 (1.4)
	(−27.1)	(−14.1)	(−8.8)	(−8.0)	(−29.9)
			$\theta^0 = 60$		
High	151.5 (0.1)	151.6 (0.1)	149.9 (0.2)	152.5 (0.1)	144.5 (0.2)
	(−3.9)	(−3.3)	(−3.6)	(−2.6)	(−2.0)
Middle	407.5 (4.2)	409.7 (−1.4)	339.4 (6.7)	352.2 (3.1)	242.8 (0.6)
	(−38.7)	(−5.9)	(−24.7)	(−1.1)	(−18.3)
Low	373.1 (4.5)	377.2 (−0.8)	317.0 (4.3)	329.9 (1.2)	230.4 (0.7)
	(−32.7)	(−4.7)	(−17.6)	(−2.6)	(−15.2)
			F^- at surface		
			$\theta^0 = 0$		
High	1075.8 (0.0)	1075.8 (0.0)	1076.8 (0.1)	1074.6 (0.0)	1081.3 (0.0)
	(5.0)	(5.3)	(5.5)	(4.2)	(3.8)
Middle	410.9 (−7.2)	410.9 (−15.0)	585.5 (−25.2)	539.2 (−11.2)	819.9 (−1.0)
	(14.6)	(18.8)	(−1.8)	(1.7)	(29.5)
Low	440.9 (−9.9)	440.4 (−16.3)	595.4 (−38.3)	546.6 (−4.6)	829.2 (−1.3)
	(9.6)	(16.4)	(−11.1)	(8.4)	(25.9)
			$\theta^0 = 60$		
High	478.7 (−0.1)	478.7 (−0.1)	480.7 (−0.2)	477.5 (−0.1)	487.4 (−0.2)
	(4.2)	(3.6)	(3.9)	(2.8)	(2.3)
Middle	165.8 (6.2)	165.8 (−5.1)	250.2 (−6.6)	234.3 (−4.0)	367.4 (−0.3)
	(25.3)	(6.5)	(12.4)	(0.6)	(14.9)
Low	175.5 (5.2)	175.6 (−5.6)	253.2 (−3.8)	236.7 (−1.6)	370.4 (−0.4)
	(24.6)	(5.5)	(8.4)	(2.8)	(13.5)

See text for further explanation.

Next, we address the performance of the algorithms for cases with three randomly overlapped cloud blocks (low, middle and high cloud) in a GCM column. The cloud fractions for each cloud block are indicated by shading in Fig. 4. Cloud fraction is assumed to be vertically constant within each cloud block. The individual clouds are resolved into several identical sub-layers, each 250 m thick. The cloud optical properties are the same as in Fig. 3 and ICA benchmark calculations are based on $N = 10\,000$.

Three cloud cases (ran1, ran2 and ran3) are considered in Fig. 4. It is noted that the cloud matrix method does not perform well. Absolute errors reaching 16 K d^{-1}, and relative errors often exceeding 40%. Furthermore, negative heating rates occur frequently. Errors in downward short-wave flux at the surface are also large, with a maximum error of 155 W m^{-2}.

For the QMC method, errors are dramatically reduced in comparison with the cloud matrix method. Absolute heating-rate errors are well below 1 K d^{-1} and relative errors

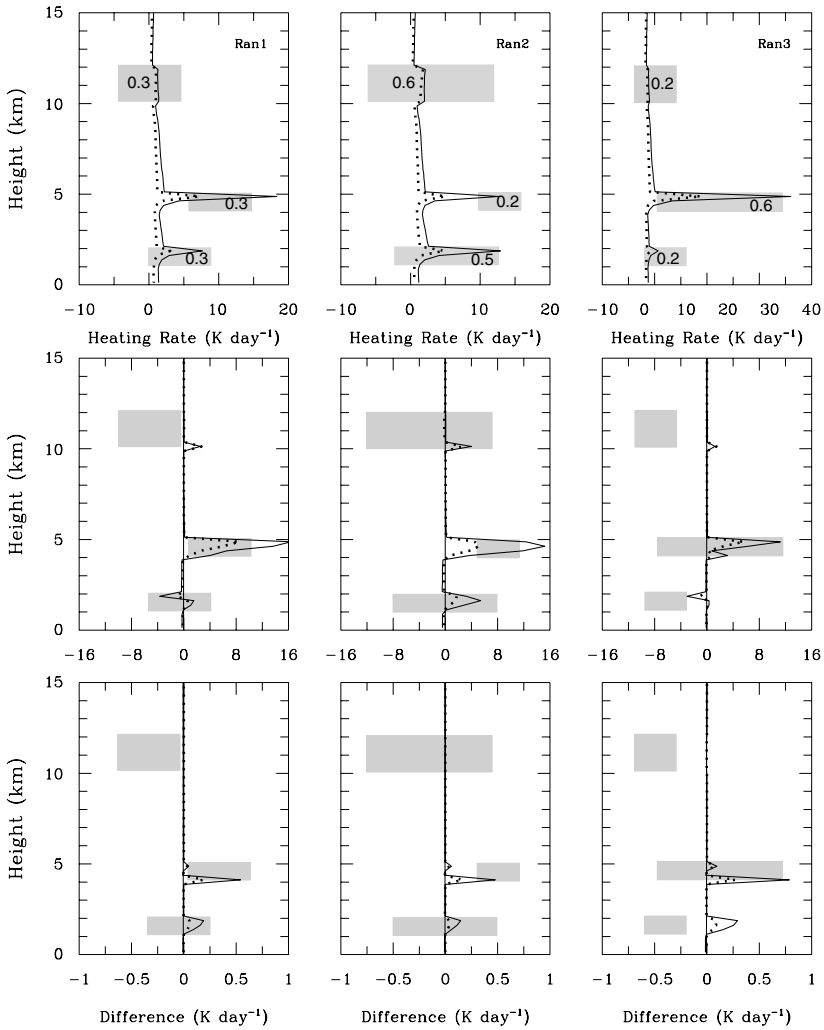

Figure 4. Top panels show the heating-rate profiles for three cloud cases of ran1, ran2, and ran3 from the benchmark results with $N = 10\,000$ ICA calculations. The clouds are in full random overlap. The cloud fractions are shown inside the shaded areas. The middle panels show the differences in the heating rate between the cloud matrix method and the benchmark ICA. The bottom panels show the differences in the heating rates between QMC and the benchmark ICA. The solid lines are the results for solar zenith angle 0° and the dotted lines are results for solar zenith angle 60°.

are less than 2%. radiative-flux errors are also very small, with a maximum error of 3 W m^{-2} (see Table 2).

In order to assure QMC will work in most situations, more complex tests are considered by combining the cloud cases in Figs. 3 and 4 together. Figure 5 is the same as Fig. 4 but replacing the individual cloud blocks in Fig. 4 with the various cloud configurations A–D shown in Fig. 3. The error in heating rate is shown in Fig. 5 enhanced for QMC since the error for each individual cloud configuration is brought in. The error in heating rate now could be up to 5 K d^{-1}. The worst case occurs for the middle cloud in ran3. As shown in Fig. 3, the error for such a configuration as C is large. The change in error for the cloud matrix method is small since the cloud matrix method

TABLE 2. COMPARISONS OF UPWARD AND DOWNWARD FLUXES (W m^{-2}) AT THE TOA AND AT THE SURFACE FOR RANDOM OVERLAP CLOUD FIELDS OF RAN1, RAN2 AND RAN3, AT SOLAR ZENITH ANGLES 0° AND 60°. FOR EACH CASE, THE NUMBER ON THE LEFT IS THE BENCHMARK ICA RESULT, THE UPPER NUMBER IN PARENTHESES IS THE ERROR FOR THE CLOUD MATRIX METHOD COMPARED TO ICA, AND THE LOWER NUMBER IN PARENTHESES IS THE ERROR FOR THE QMC MODEL (W m^{-2}).

	$\theta^0 = 0$		$\theta^0 = 60$	
Cloud	F^+(TOA)	F^-(surface)	F^+(TOA)	F^-(surface)
ran1	600.8 (−3.2)	595.5 (−94.2)	322.6 (−0.8)	260.7 (−43.3)
	(−1.3)	(−1.6)	(−0.5)	(−0.4)
ran2	651.1 (−0.6)	511.4 (−155.0)	350.8 (27.2)	218.4 (−81.7)
	(−0.9)	(−1.6)	(−0.4)	(−0.4)
ran3	733.4 (−3.2)	430.5 (−40.6)	388.4 (−1.3)	185.5 (−18.7)
	(−1.8)	(−2.7)	(−0.7)	(−0.9)

See text for further explanation.

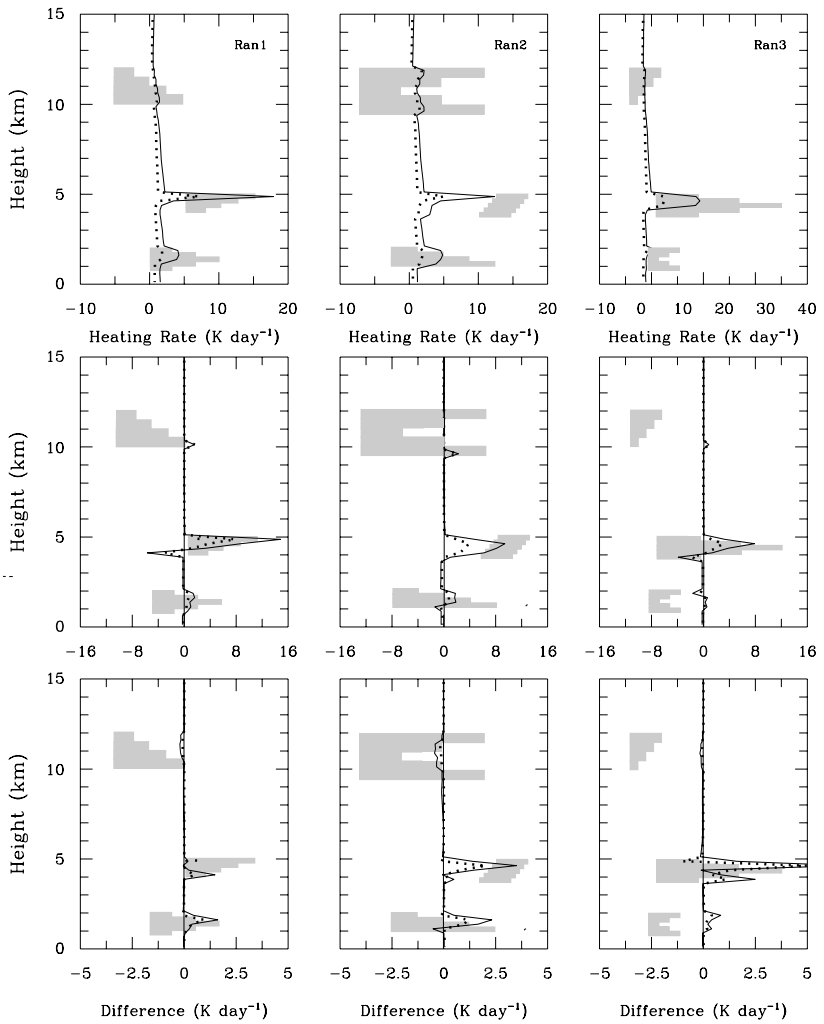

Figure 5. The same as Fig. 4 but replacing the individual cloud blocks in Fig. 4 with the various cloud configurations A–D shown in Fig. 3.

TABLE 3. THE SAME AS TABLE 2 BUT CORRESPONDING TO FIG. 5 FOR EACH CLOUD BLOCK WITH CONFIGURATIONS A–D (cf. FIG. 3). FOR EACH CASE, THE NUMBER ON THE LEFT IS THE BENCHMARK ICA RESULT, THE UPPER NUMBER IN PARENTHESES IS THE ERROR FOR THE CLOUD MATRIX METHOD COMPARED TO ICA, AND THE LOWER NUMBER IN PARENTHESES IS THE ERROR FOR THE QMC MODEL (W m^{-2}).

	$\theta^0 = 0$		$\theta^0 = 60$	
Cloud	F^+(TOA)	F^-(surface)	F^+(TOA)	F^-(surface)
ran1	558.3 (15.4)	652.4 (−93.2)	305.7 (6.7)	282.2 (−41.5)
	(−13.0)	(1.6)	(−9.9)	(5.1)
ran2	643.5 (41.2)	523.0 (−138.9)	352.3 (21.3)	217.7 (−60.4)
	(−42.7)	(11.3)	(−28.4)	(18.9)
ran3	686.7 (27.9)	489.4 (−62.9)	370.9 (10.3)	206.7 (−23.9)
	(−29.2)	(−0.3)	(−26.3)	(−10.3)

See text for further explanation.

could handle each cloud configuration accurately. However, generally the results for QMC are still much better than those for the cloud matrix method. Correspondingly the errors in flux for QMC are enhanced (see Table 3) with a maximum of 8% for the ran3 case.

In summary, the cloud matrix method performs somewhat better than the QMC method with approximation (7) for individual cloud blocks that are close to maximum overlap. For cases with random overlap, the QMC method provides quite good results whereas the cloud matrix method gives significant errors.

(*b*) *Cloud subgrid variability*

Cloud subgrid variability refers to horizontal variations within each cloud block, and it is thus a distinctly different concept from cloud overlap, which emphasizes the vertical correlation between cloud blocks.

In Fig. 6, three overcast cloud blocks are considered: high, middle, and low. Cloud optical properties are the same as those used in the previous subsection. Stripes of different grey scale in Fig. 6 characterize the horizontal inhomogeneity of the clouds. The vertical alignment of the stripes signifies that cloud horizontal variations are assumed to be perfectly correlated in the vertical within each cloud block.

On the left of Fig. 6 are homogeneous cloud heating-rate profiles for the three cases. Also shown are heating-rate differences to ICA benchmark results for two 1-D models: for the horizontally homogeneous cloud model and for the inhomogeneous cloud model using (12). The ICA values were obtained by explicit integration of the 1-D homogeneous model weighted by the appropriate gamma distribution in (10). For low and middle clouds, the homogeneous model dramatically overestimates heating near the cloud top. For $\nu = 0.5$, the errors can be about 20 K d^{-1}. However, based on our parametrization of (12), errors are greatly reduced, less than 2 K d^{-1} in most cases.

Table 4 lists the upward flux at the TOA and downward flux at the surface that correspond to the plots in Fig. 6 for two different solar zenith angles. The errors for the homogeneous model cloud can be very large for $\nu = 0.5$, especially for the downward flux at the surface. The downward flux at the surface for the inhomogeneous cloud can be about three times larger than that for the corresponding homogeneous model. Even for $\nu = 2$, the relative errors can be about 35% for the homogeneous model. However, based on our parameterization, errors for the upward and downward fluxes decrease dramatically irrespective of ν and generally errors are less than 1%.

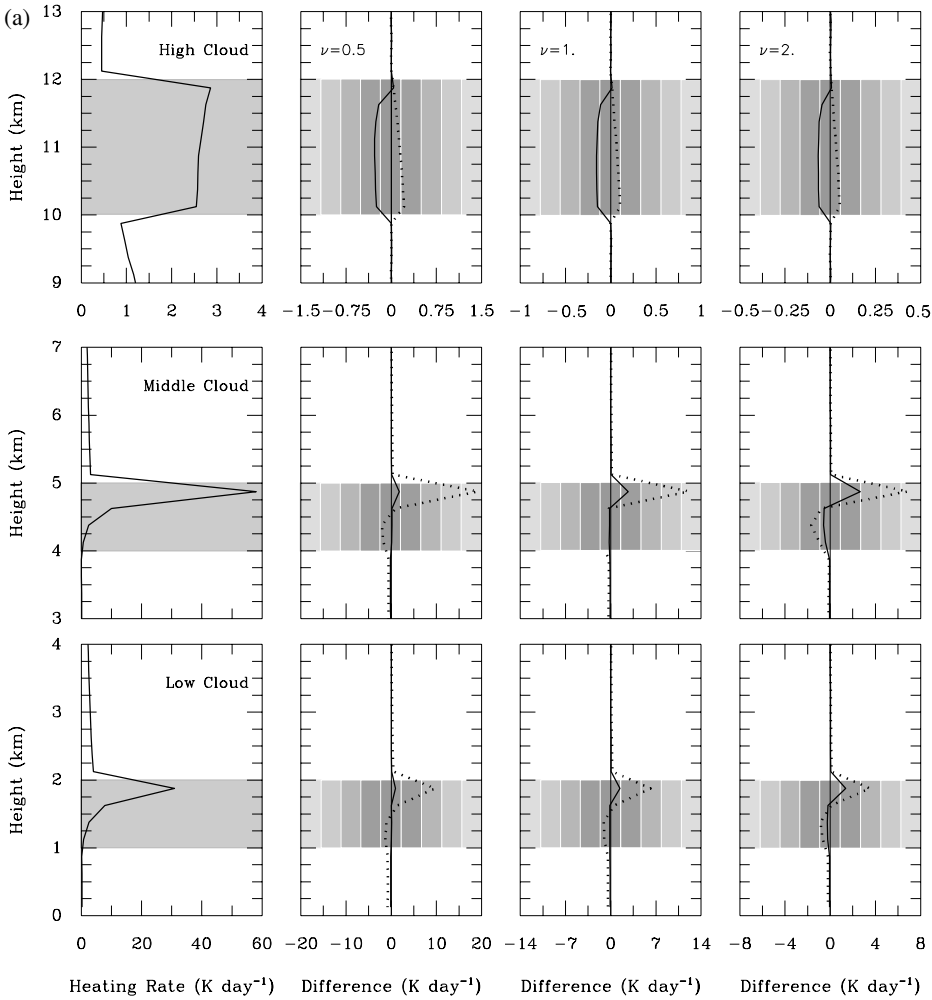

Figure 6. Left column shows heating-rate profiles for homogeneous clouds. Shaded regions indicate cloud position. The stripes with different darkness indicate horizontal inhomogeneity. The other columns show heating-rate differences between two 1-D models and benchmarks computed by the ICA for inhomogeneous clouds with variability described by ν, as listed on the plots. Solid lines are for the inhomogeneous scheme with layer correlations as defined in (12); dotted lines are for the homogeneous model. Solar zenith angle is (a) 0° and (b) 60°.

The situation is different for the high-cloud case. The horizontally homogeneous model produces very accurate heating rates (Fig. 6) that are no worse than those using our parametrization (12). In other words, the effect of subgrid-scale variability is very small. Because the cloud optical depth is small in the high-cloud case, direct transmission dominates over multiple scattering, and the difference between the exact result (power function) and the exponential (homogeneous cloud result) in (11) is small. This weak subgrid effect for high clouds can be understood from another argument that the reflectance and transmittance functions vary linearly for small optical thicknesses, so the integration of results for each weighting function point is similar to the reflectance and transmittance derived from the mean optical depth, and so inhomogeneity has little effect.

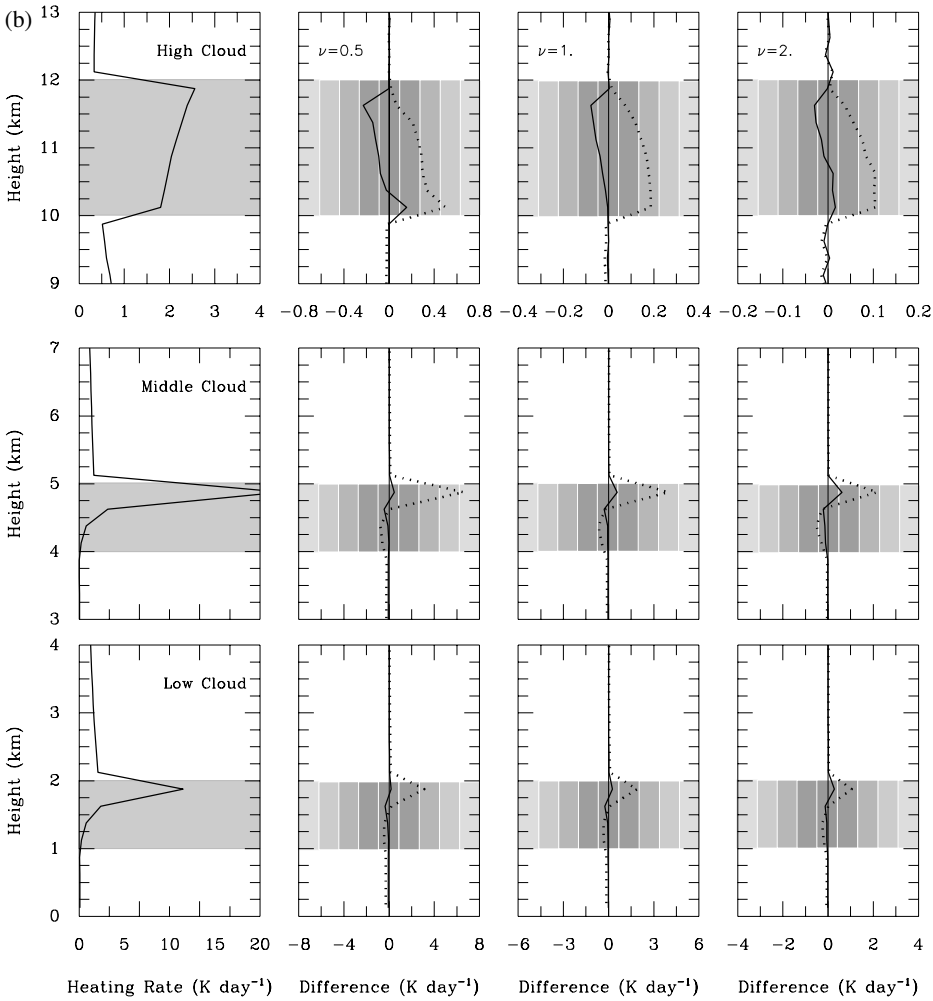

Figure 6. Continued.

TABLE 4. COMPARISONS OF UPWARD AND DOWNWARD FLUXES (W m^{-2}) AT THE TOA AND AT THE SURFACE FOR LOW AND MIDDLE CLOUDS FOR TWO SOLAR ZENITH ANGLES (0° AND 60°) AND FOR THREE VALUES OF ν. FOR EACH CASE, THE FIRST NUMBER IS THE BENCHMARK ICA RESULT, THE SECOND NUMBER (IN PARENTHESES) IS THE ERROR FOR THE INHOMOGENEOUS MODEL (12) AND THE THIRD NUMBER (IN PARENTHESES) IS THE HOMOGENEOUS MODEL ERROR.

		F^-(surface)		
		$\nu = 0.5$	$\nu = 1.0$	$\nu = 2.0$
Middle cloud	0°	402.2 (−1.0) (−269.4)	280.7 (1.7) (−147.9)	202.8 (1.0) (−70.0)
	60°	151.2 (−1.7) (−105.4)	99.7 (4.8) (−53.9)	70.2 (3.8) (−24.4)
Low cloud	0°	430.8 (−2.6) (−276.2)	311.7 (−2.9) (−157.1)	231.9 (−3.9) (−77.3)
	60°	161.5 (−3.8) (−108.4)	110.4 (2.7) (−57.3)	79.9 (2.2) (−26.8)
		F^+(TOA)		
		$\nu = 0.5$	$\nu = 1.0$	$\nu = 2.0$
Middle cloud	0°	757.9 (0.9) (207.2)	850.4 (−2.3) (114.7)	910.3 (−1.5) (54.8)
	60°	422.2 (4.5) (84.3)	463.7 (−3.1) (42.8)	487.2 (−3.1) (19.3)
Low cloud	0°	695.2 (−0.6) (194.4)	777.9 (0.0) (111.7)	834.0 (1.5) (55.6)
	60°	387.3 (4.7) (79.5)	425.0 (−1.7) (41.8)	447.3 (−1.8) (19.5)

See text for further explanation.

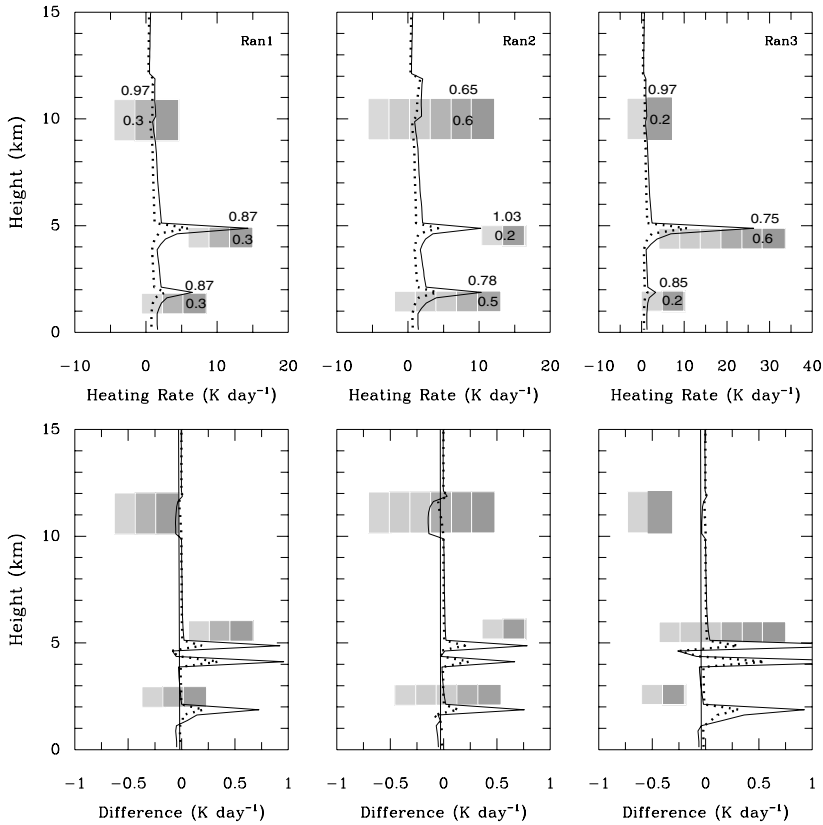

Figure 7. Top panels show the heating-rate profiles for ICA benchmark calculations for the three random overlap cases ran1, ran2 and ran3 as in Fig. 4, but with cloud subgrid-scale variability included. Layer cloud fractions are listed inside the shaded regions with the corresponding values of ν listed above them. Bottom panels show the corresponding heating-rate errors for the QMC scheme using (12). The solid lines are the results for solar zenith angle 0° and the dotted lines are results for solar zenith angle 60°. See text for further explanation.

Flux differences are not listed in Table 4 for the high-cloud case because the errors are generally smaller than a few W m^{-2}. For the inhomogenous case we don't show the results for cloud with configurations as shown in Fig. 3 for the homogenous case, we found the errors in heating rate and flux are similar to the homogenous case.

(*c*) *Fractional clouds with subgrid variability*

Figure 7 shows schematically the cloud position, cloud fraction, and subgrid-scale variability for three configurations of a cloud system containing three cloud blocks. Each cloud contains several contiguous identical sub-layers (the cloud fractions and overlap patterns are the same as Fig. 4 for the homogeneous cases). Contiguous layers are unique realizations of the cascade model and all three cloud blocks in each case are positioned in the horizontal at roughly random locations. In each case, ICA benchmarks results are averaged for 819 920 column calculations the same as those in Li and Barker (2002). Results are only shown for the QMC scheme with the inhomogeneity parametrization given by (12).

TABLE 5. COMPARISONS OF UPWARD AND DOWNWARD FLUXES (W m^{-2}) AT THE TOA AND AT THE SURFACE FOR RANDOM OVERLAP CLOUD FIELDS OF RAN1, RAN2, AND RAN3 AS IN TABLE 2, BUT NOW WITH CLOUD SUBGRID-SCALE VARIABILITY INCLUDED. FOR EACH CASE, THE FIRST NUMBER IS THE BENCHMARK ICA RESULT, THE SECOND NUMBER (IN PARENTHESES) IS THE ERROR FOR THE QMC MODEL USING (12). CORRESPONDING HEATING-RATE PLOTS ARE SHOWN IN FIG. 7.

	$\theta = 0°$		$\theta = 60°$	
Cloud	F^+(TOA)	F^-(surface)	F^+(TOA)	F^-(surface)
ran1	541.0 (−4.5)	675.3 (−1.0)	299.8 (−2.6)	290.5 (1.6)
ran2	579.0 (−3.7)	610.7 (0.2)	322.6 (−2.2)	255.9 (2.2)
ran3	643.9 (−8.0)	546.6 (−0.9)	354.4 (−4.0)	228.6 (2.2)

Heating-rate errors occur mostly in low and middle clouds. This is expected since the effect of inhomogeneity for high clouds is small by comparison. In comparison with Fig. 4 (for the homogeneous case), the errors shown in Fig. 7 are slightly larger.

Values of upward flux at the TOA and downward flux at the surface and corresponding errors relative to benchmark calculations are listed in Table 5. The maximum error in flux is only about 8 W m^{-2} or 1.2%. If inhomogeneity is neglected, the errors can exceed 100 W m^{-2} for the same cloud overlap patterns (cf. Table 2).

6. CONCLUSION

There is a strong push for climate models to address such problems as the cloud feedback issue or the climate impact of aerosols. To resolve such questions, the sensitivity of the GCMs to systematic changes in the radiative properties of a few W m^{-2} is necessary. We note in this paper that the error in radiative properties introduced by assumptions of overlap and inhomogeneity can greatly exceed this threshold. In fact, we find that in some representative cases studied the errors introduced by commonly used overlap schemes in current GCMs can be as much as 155 W m^{-2} for fluxes and more than 16 K d^{-1} for heating rates. A subgrid multi-column approach circumvents this problem but can become computationally expensive for large numbers of columns.

In this paper, we outline a new approach to the treatment of overlap and inhomogeneity at solar wavelengths. Each element of the treatment is systematically tested versus ICA benchmarking calculations. For cases with random overlap and inhomogeneous clouds, up to 800 000 columns were used for benchmarking comparisons with cloud arrangements generated by a cascade model. We are not aware of any such previous comparisons for other cloud overlap treatments.

We have developed a simplified quasi multi-column approach to the overlap problem. It has almost as good accuracy as the multi-column approach but has only a maximum of four columns (one clear and three cloudy). Incorporated into the QMC approach is a proper algorithm for the treatment of the coupling of the upward and downward fluxes that can handle overlap. We show that, for clouds treated in three vertical regions, low, middle, and high, this QMC approach yields reasonably accurate results for the fluxes and heating rates. We further simplify each cloud block (low, middle, high) to have a single cloud fraction and provide an algorithm to calculate it from the overlap circumstances.

For subgrid cloud inhomogeneity at solar wavelengths, the use of the gamma distribution of optical depth in radiative transfer cannot be simplified in the same way as for the infrared due to the complications imposed by scattering. We therefore propose

the use of an optical-depth adjustment algorithm. This approach is computationally fast and so can be easily incorporated into the overlap scheme that was developed.

In summary, the new algorithm combines relaxed maximum random overlap, scaling of the optical depth for cloud inhomogeneity, QMC approach for overlap, and scaling of the cloud fraction within cloud blocks. This approach can produce accurate results in heating rates and fluxes with relative errors generally less than 8%. Importantly, this accuracy is achieved at a computational expense that is quite appropriate for GCMs. This radiative-transfer algorithm is available from the authors.

ACKNOWLEDGEMENTS

The authors would like to thank Dr H. Barker and Dr R. J. Hogan for helpful discussions and three anonymous reviewers for helpful comments.

APPENDIX A

Adding method for solar radiative transfer

We interpret the adding process for the radiative-transfer process (based on Coakley *et al.* 1983) so as to make it easier for the reader to understand the cloud treatment discussed in this paper. We find the description of the adding process in some previous papers was not very clear, since the upward and downward reflection and transmission for multiple layers were not written down specifically.

For each single layer i, the layer diffuse reflection $\overline{r}_i$ and transmission $\overline{t}_i$ are the solution of the radiative-transfer equation with no direct solar source term.

$$\overline{r}_i = (u+1)(u-1)(\mathrm{e}^{\lambda\tau_i} - \mathrm{e}^{-\lambda\tau_i})N^{-1}, \tag{A.1}$$

$$\overline{t}_i = 4uN^{-1} \tag{A.2}$$

where

$$N = (u+1)^2\,\mathrm{e}^{\lambda\tau_i} - (u-1)^2\,\mathrm{e}^{-\lambda\tau_i},$$

$$u = \tfrac{3}{2}\frac{1-\omega_i g_i}{\lambda},$$

$$\lambda = \sqrt{3(1-\omega_i)(1-\omega_i g_i)},$$

with τ_i, ω_i and g_i being the optical depth, single scattering albedo and asymmetry factor for layer i, respectively. The direct layer reflection $r_i(\mu_0)$ and direct layer transmission $t_i(\mu_0)$ are the solution for the full radiative-transfer equation,

$$r_i(\mu_0) = (\alpha-\gamma)(\overline{t}_i\,\mathrm{e}^{-\tau_i/\mu_0} - 1) + (\alpha+\gamma)\overline{r}_i, \tag{A.3}$$

$$t_i(\mu_0) = (\alpha-\gamma)\overline{r}_i\,\mathrm{e}^{-\tau_i/\mu_0} + (\alpha+\gamma)(\overline{t}_i - \mathrm{e}^{-\tau_i/\mu_0}) + \mathrm{e}^{-\tau_i/\mu_0}, \tag{A.4}$$

where μ_0 is the cosine of solar zenith angle and

$$\alpha = \tfrac{3}{4}\omega_i\mu_0\left\{\frac{1+g_i(1-\omega_i)}{1-\lambda^2\mu_0^2}\right\},$$

$$\gamma = \tfrac{1}{2}\omega_i\left\{\frac{1+3g_i(1-\omega_i)\mu_0^2}{1-\lambda^2\mu_0^2}\right\}.$$

The reflectivity for diffuse radiation for an atmospheric slab extending from the TOA to the level k is obtained through a downward path calculation as

$$\overline{R}_{1,k} = \overline{r}_{k-1} + \frac{\overline{t}_{k-1}\overline{R}_{1,k-1}\overline{t}_{k-1}}{1 - \overline{r}_{k-1}\overline{R}_{1,k-1}}, \tag{A.5}$$

and the transmissivity for direct solar radiation is

$$T_{1,k}(\mu_0) = \mathrm{e}^{-\tau_{1,k-1}/\mu_0} t_{k-1}(\mu_0) + \frac{\overline{t}_{k-1}\{T_{1,k-1}(\mu_0) - \mathrm{e}^{-\tau_{1,k-1}/\mu_0}(1 - r_{k-1}(\mu_0))\}\overline{R}_{1,k-1}}{1 - \overline{r}_{k-1}\overline{R}_{1,k-1}}, \tag{A.6}$$

where $\tau_{1,k-1} = \sum_{i=1}^{k-2} \tau_i$.

For an atmospheric slab extending from the surface to the level k, the reflectivities for diffuse radiation ($\overline{R}_{N,k}$) and direct solar radiation ($R_{N,k}(\mu_0)$) are obtained through an upward path calculation as

$$\overline{R}_{N,k} = \overline{r}_k + \frac{\overline{t}_k\overline{R}_{N,k+1}\overline{t}_k}{1 - \overline{r}_k\overline{R}_{N,k+1}}, \tag{A.7}$$

$$R_{N,k}(\mu_0) = r_k(\mu_0) + \frac{\overline{t}_k\{(t_k(\mu_0) - \mathrm{e}^{-\tau_k/\mu_0})\overline{R}_{N,k+1} + \mathrm{e}^{-\tau_k/\mu_0}R_{N,k+1}(\mu_0)\}}{1 - \overline{r}_k R_{N,k+1}}. \tag{A.8}$$

$\overline{R}_{N,N} = R_{N,N}(\mu_0) =$ surface albedo. Finally, the downward and upward fluxes at level k are determined by the results from the downward and upward calculation paths as follows:

$$F_k^- = \mathrm{e}^{-\tau_{1,k}/\mu_0} + \frac{T_{1,k}(\mu_0) - \mathrm{e}^{-\tau_{1,k}/\mu_0}(1 - R_{N,k}(\mu_0)\overline{R}_{1,k})}{1 - \overline{R}_{1,k}\overline{R}_{N,k}}, \tag{A.9}$$

$$F_k^+ = \frac{(T_{1,k}(\mu_0) - \mathrm{e}^{-\tau_{1,k}/\mu_0})\overline{R}_{1,k} + \mathrm{e}^{-\tau_{1,k}/\mu_0}R_{1,k}(\mu_0)}{1 - \overline{R}_{1,k}\overline{R}_{N,k}}. \tag{A.10}$$

References

Barker, H. W. 1996 A parameterization for computing grid-averaged solar fluxes for inhomogeneous marine boundary layer clouds. Part I: Methodology, and homogeneous biases. *J. Atmos. Sci.*, **53,** 2298–2303

Barker, H. W., Stephens, G. L. and Fu, Q 1999 The sensitivity of domain-averaged solar fluxes to assumptions about cloud geometry. *Q. J. R. Meteorol. Soc.*, **125,** 2127–2152

Bergman, J. W. and Rasch, P. J. 2002 Parameterizing vertically coherent cloud distributions. *J. Atmos. Sci.*, **59,** 2165–2182

Cahalan, R. F., Ridgway, W., Wiscombe, W. J., Bell, T. L. and Snider, J. B. 1994 The albedo of fractal stratocumulus clouds. *J. Atmos. Sci.*, **51,** 2434–2455

Coakley, J. A., Cess, R. D. and Yurevich, F. B. 1983 The effect of tropospheric aerosols on the Earth's radiation budget: A parameterization for climate models. *J. Atmos. Sci.*, **40,** 116–138

Collins, W. D. 2001 Parameterization of generalized cloud overlap for radiative transfer calculations in general circulation models. *J. Atmos. Sci.*, **58,** 3224–3242

Dobbie, J. S., Li, J. and Chýlek, P. 1999 Two and four stream optical properties for water clouds and solar wavelengths. *J. Geophys. Res.*, **104,** 2067–2079

Fouquart, Y. and Bonnel, B. 1980 Computations of solar heating of the earth's atmosphere: a new parameterization. *Beitr. Phys. Atmos.*, **53,** 35–62

Fu, Q. 1996 An accurate parameterization of the infrared radiative properties of cirrus clouds for climate models. *J. Climate*, **11,** 2223–2337

Geleyn, J.-F. and Hollingsworth, A. 1979 An economical analytical method for the computation of the interaction between scattering and line absorption of radiation. *Beitr. Phys. Atmos.*, **52,** 1–16

Harshvardhan, Davies, R., Randall, D. A. and Corsetti, T. G. 1987 A fast radiation parameterization for atmospheric circulation models. *J. Geophys. Res.*, **92,** 1009–1016

Hogan, R. J. and Illingworth, A. J. 2000 Deriving cloud overlap statistics from radar. *Q. J. R. Meteorol. Soc.*, **126,** 2903–2909

2003 Parameterizing ice cloud inhomogeneity and the overlap of inhomogeneities using cloud radar data. *J. Atmos. Sci.*, **60,** 756–767

IPCC 1996 'Climate Change 1995: The Science of Climate Change'. Eds. J. T. Houghton, F. G. Meira Filho, B. A. Callander, N. Harris, A. Kattenberg and K. Maskell. Cambridge University Press

2001 'Climate Change 2001. The scientific basis'. Eds. J. T. Houghton, Y. Ding, M. Nogua, D. Griggs, P. Vander Linden and K. Maskell. Cambridge University Press

Jakob, C. 2002 'Ice clouds in numerical weather prediction models—progress, problems, and prospects'. In *Cirrus*. Eds. D. K. Lynch, K. Sassen, D. O'C. Starr and G. Stephens. Oxford University Press

Jakob, C. and Klein, S. A. 1999 The role of vertically varying cloud fraction in the parameterization of microphysical processes in the ECMWF model. *Q. J. R. Meteorol. Soc.*, **125A,** 941–965

Kato, S. 2003 Computation of domain-averaged shortwave irradiance by a one-dimensional algorithm incorporating correlations between optical thickness and direct incident radiation. *J. Atmos. Sci.*, **60,** 182–193

Li, J. 2000 Accounting for overlap of fractional cloud in infrared radiation. *Q. J. R. Meteorol. Soc.*, **126,** 3325–3342

2002 Accounting for unresolved clouds in a 1D infrared radiative transfer model. Part I: Solution for radiative transfer, cloud scattering, and overlap. *J. Atmos. Sci.*, **59,** 3302–3320

Li, J. and Barker, H. W. 2002 Accounting for unresolved clouds in a 1D infrared radiative transfer model. Part II: horizontal variability of cloud water path. *J. Atmos. Sci.*, **59,** 3321–3339

2005 A radiation algorithm with correlated k-distribution. Part I: local thermal equilibrium. *J. Atmos. Sci.*, **60,** 286–309

Liang, X.-Z. and Wang, W.-C. 1997 Cloud overlap effects on GCM climate simulations. *J. Geophys. Res.*, **102,** 11039–11047

Liou, K-N. 1986 Influence of cirrus clouds on weather and climate processes: A global perspective. *Mon. Weather Rev.*, **114,** 1167–1199

Los, A. and Duynkerke, P. G. 2001 Parameterization of solar radiation in inhomogeneous stratocumulus: Albedo bias. *Q. J. R. Meteorol. Soc.*, **127,** 1593–1614

McClatchey, R. A., Fenn, R. W., Selby, J. E. A., Volz, F. E. and Garing, J. S. 1972 *Optical properties of the atmosphere.* 3rd edition, AFCRL-72-0497 [NTIS N7318412]

Mace, G. G. and Benson-Troth, S. 2002 Cloud-layer overlap characteristics derived from long-term cloud radar data. *J. Climate*, **15,** 2505–2515

Manabe, S. and Strickler, R. 1964 Thermal equilibrium of the atmosphere with a convective adjustment. *J. Atmos. Sci.*, **21,** 361–385

Morcrette, J.-J. and Fouquart, Y. 1986 The overlapping of cloud layers in shortwave radiation parameterizations. *J. Atmos. Sci.*, **43,** 321–328

Morcrette, J. J. and Jakob, C. 2000 The response of the ECMWF model to changes in the cloud overlap assumption. *Mon. Weather Rev.*, **128,** 1707–1732

Oreopoulos, L. and Barker, H. W. 1999 Accounting for subgrid-scale cloud variability in a multi-layer, 1D solar radiative transfer algorithm. *Q. J. R. Meteorol. Soc.*, **125,** 301–330

Räisänen, P. 1998 Effective longwave cloud fraction and maximum-random overlap of clouds: A problem and a solution. *Mon. Weather Rev.*, **126,** 3336–3340

Räisänen, P., Barker, H. W., Khairoutdinov, M., Li, J. and Randall, D. 2004 Stochastic generation of subgrid-scale cloudy columns for large-scale models. *Q. J. R. Meteorol. Soc.*, **130,** 2047–2068

Stubenrauch, C. J., Del Genio, A. D. and Rossow, W. B. 1997 Implementation of subgrid cloud vertical structure inside a GCM and its effect on the radiation budget. *J. Climate*, **10,** 273–287